

Ultra-high Photoresponsivity of Gold Nanodisk Array/CVD MoS₂-based Hybrid Phototransistor

Shyam Narayan Singh Yadav¹, Po-Liang Chen², Yu-Chi Yao³, Yen-Yu Wang^{4,5}, Der-Hsien Lien⁶, Yu-Jung L^{4,5}, Ya-Ping Hsieh³, Chang-Hua Liu^{2,7}, and Ta-Jen Yen^{1}*

¹Department of Materials Science and Engineering, National Tsing Hua University, Hsinchu 300, Taiwan R.O.C.

²Institutes of Photonics Technology, National Tsing Hua University, Hsinchu, 30013, Taiwan

³Institute of Atomic and Molecular Sciences, Academia Sinica, Taipei, 10617, Taiwan, R.O.C.

⁴Department of Physics, National Taiwan University, Taipei 106, Taiwan R.O.C.

⁵Research Center for Applied Sciences, Academia Sinica, Taipei 115, Taiwan R.O.C.

⁶Department of Electrical Engineering, National Yang-Ming Chao Tung University, Hsinchu, 300, Taiwan, R.O.C.

⁷Department of Electrical Engineering, National Tsing Hua University, Hsinchu, 30013, Taiwan

Corresponding Author

Email: tjyen@mx.nthu.edu.tw

Keywords: CVD monolayer MoS₂, localized surface plasmons, light-matter interactions, hybrid visible photodetectors

Abstract

Owing to its atomically thin thickness, layer-dependent tunable band gap, flexibility, and CMOS compatibility, MoS₂ is a promising candidate for photodetection. However, monolayer MoS₂-based photodetectors typically show poor optoelectronic performances, mainly limited by their low optical absorption. In this work, we hybridized CVD-grown monolayer MoS₂ with a gold nanodisk (AuND) array to demonstrate a superior visible photodetector through a synergetic effect. It is evident from our experimental results that there is a strong light-matter interaction between AuNDs and monolayer MoS₂, which results in better photodetection due to a surface trap state passivation with a longer charge carrier lifetime compared to pristine MoS₂. In particular, the AuND/MoS₂ system demonstrated a photoresponsivity of $8.7 \times 10^4 \text{ AW}^{-1}$, specific detectivity of $6.9 \times 10^{13} \text{ Jones}$, and gain 1.7×10^5 at $31.84 \mu\text{Wcm}^{-2}$ illumination power density of 632 nm wavelength with an applied voltage of 4.0 V for an AuND/MoS₂-based photodetector. To our knowledge, these optoelectronic responses are one order higher than reported results for CVD MoS₂-based photodetector in the literature.

1. Introduction

Conversion of the optical signal into an electrical signal has become a hot topic of research due to its high demands in various fields e.g. video imaging, biomedical imaging, gas sensing, and motion detection.¹ Although this field becomes mature due to the development of high-performance materials and integration technology, still there is a need for high-performance photodetection devices with complementary metal oxide semiconductor (CMOS) compatibility at sub-10-nm technology nodes.² Among the many materials being investigated for potential use in photoactive channels, transition metal dichalcogenides (TMDCs) have gained considerable attention because of their sub-nm thickness and lack of dangling bonds at the dielectric interface.^{3, 4} In addition, TMDCs possess thickness-dependent bandgap from 1.0 to 2.5 eV,⁵⁻⁸ high electron mobility ($200 \text{ cm}^2\text{V}^{-1}\text{S}^{-1}$),⁹ and excellent current ON/OFF ratio ($\approx 10^8$),¹⁰ thriving to be a promising candidate for photodetector.¹¹⁻¹⁴ Despite these superior optical and electrical qualities, the monolayer MoS_2 is intrinsically limited by its low optical absorption (5%),¹⁵ due to its atomically thin layer. On the other hand, bulk MoS_2 possesses an indirect bandgap,¹⁶ which is not suitable for photodetection applications. Therefore, those TMDCs-based photodetectors can only reach the maximum responsivity and gain up to the order of $2.2 \times 10^3 \text{ AW}^{-1}$ and 10^3 , respectively in the case of CVD-grown MoS_2 .¹⁷⁻²⁰

To further improve the photoresponsivity of a monolayer MoS_2 -based photodetector, researchers demonstrated various methods e.g. making heterostructures,^{21, 22} and hybridizing with waveguides,²³⁻²⁵ Although heterostructures and waveguides integrated MoS_2 -based reported work shows considerably high photoresponsivity, enabling a strong light-matter interaction still offer potentials to improve optoelectronic responses.^{19, 26-28} By employing a similar mechanism, in this work, we have designed and fabricated an gold nanodisk (AuND) array having localized surface plasmon resonance (LSPR) in the visible region (660 nm) near the band edge of monolayer MoS_2 as illustrated by our FDTD simulation and UV-Vis measurement results. Furthermore, we have hybridized a CVD-grown monolayer MoS_2 with a

AuND array on SiO₂/Si substrate and characterized their optical properties. Finally, the optoelectronic properties of the designed phototransistors were probed and observed that the AuND/MoS₂ hybrid phototransistor outperformed the MoS₂ phototransistor owing to the LSPR induced synergetic enhancement. The maximum responsivity of $8.7 \times 10^4 \text{ AW}^{-1}$, detectivity of $6.9 \times 10^{13} \text{ Jones}$, and gain of 1.7×10^5 at $31.84 \mu\text{Wcm}^{-2}$ illumination power density of 632 nm wavelength with an applied voltage of 4.0 V were achieved. Furthermore, the fabricated phototransistor scrutinized of its broadband response, revealing its capability to exhibit photo response across the entire visible spectrum. Based on our knowledge, the demonstrated optoelectronic performance of our designed AuND/MoS₂ phototransistor is enhanced in contrast to the presented results in the literature.¹⁷⁻²⁰

2. Results and Discussion

Our hybrid photodetector is comprised of CVD-grown monolayer MoS₂, beneath an array of AuND, as illustrated in **Figure 1a**. In this hybrid photodetector, MoS₂ functions as a photoactive channel layer, and AuND as a plasmonic structure that improves light-matter interaction by enabling LSPR in its vicinity resulting in an enhancement in hot electron injection efficiency²⁹ as well as photodetector performance.^{20, 30-33} The synthesis of monolayer MoS₂ and fabrication of AuND array is detailed in the **Experimental Methods**. To design the plasmonic structure a parameter sweep at fixed periodicity for variable AuND diameter was run using finite difference time domain (FDTD) simulation using commercial Lumerical[®] software (refer to **Experimental Methods** for simulation details) and is shown in Figure 1b. From Figure 1b, it is evident that at a diameter size of 90 nm, the reflectance reaches its maximum at the 660 nm wavelength which is also the PL peak of monolayer MoS₂. The electric field distribution at resonance wavelength (660 nm) was plotted and x-z is the view shown in Figure 1c, illustrating that the field is highly confined around the edge of the designed AuND owing to induced LSPR at resonance wavelength. The z- component of the x-z view, x-y view, and normal x-y view are

shown in Figure S1 (Supporting Information). The z-component of field distribution in Figures S1a and S1c depict the dipole formation due to incident E-field at AuND.

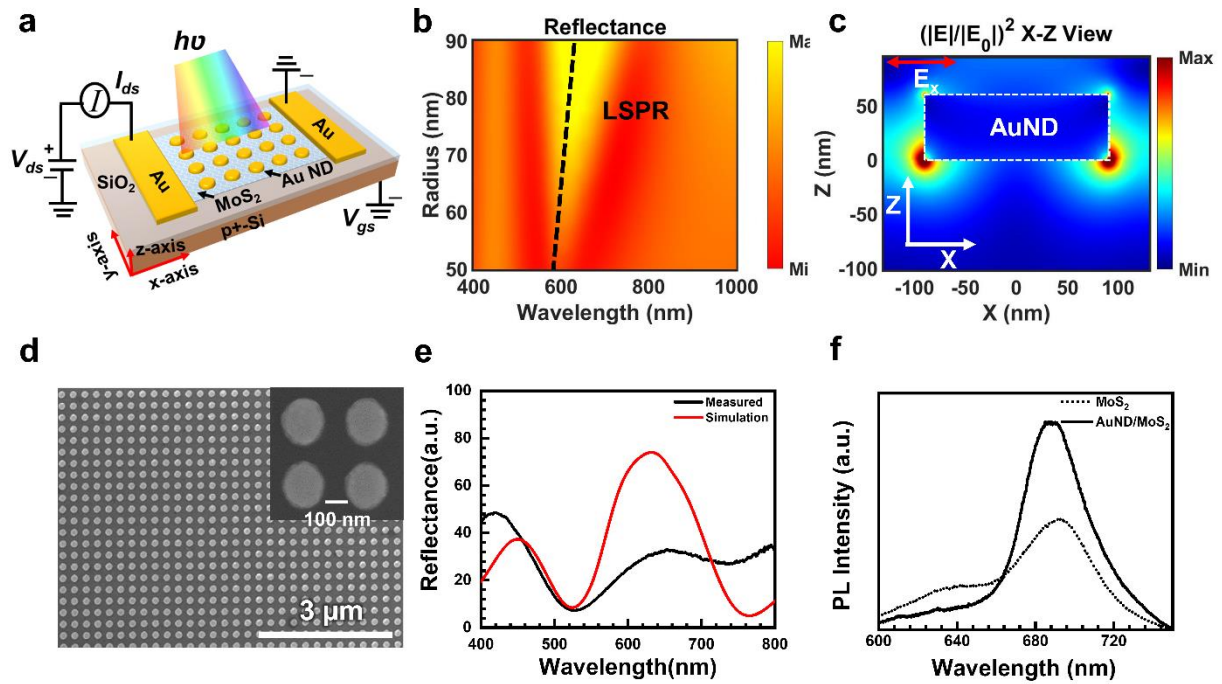


Figure 1: (a) The schematic illustration of the AuND array/MoS₂ hybrid photodetector device, the inset image shows the fabricated device. (b) Au NDs array parameter optimization. (c) Electric Field E₂ distribution in XZ plane (d) SEM image of fabricated Au ND array, the inset image shows enlarge image. (e) Simulated and measured reflectance spectra of designed AuND array. (f) Measurement photoluminescence of pristine MoS₂ and AuND/MoS₂.

Next, we fabricated the designed AuND array (for fabrication details see **Experimental Methods**). The field emission scanning electron microscopy (FESEM) image of the fabricated AuND array is shown in Figure 1d. It is observed that the size parameters of the fabricated AuND array are well-matched with the designed AuND. Furthermore, the reflectance spectra of the fabricated AuND array were measured using a micro-UV spectrometer and are exhibited in Figure 1e. It is observed that measured reflectance spectra matched well with FDTD-simulated reflectance spectra. In addition, to scrutinize the optical properties of monolayer MoS₂ and AuND/MoS₂ hybrid structure the UV-Vis absorbance spectra, Raman spectra, and

photoluminescence (PL) were measured. The measured raman spectra and absorbance are shown in Figure S2 (Supporting Information). Figure S2a depicts that the two Raman peaks, namely E_{2g}^1 and A_{1g} active modes, exhibit nearly 385.64 cm^{-1} and 404.74 cm^{-1} , respectively. The difference between these two peaks is calculated and found to be less than 20 cm^{-1} , corresponding to monolayer MoS_2 .³⁴⁻³⁶ Furthermore, Figure S2b depicts that the absorbance of MoS_2 was enhanced after hybridization with AuND array with resonance peak visible at 660 nm wavelength. This enhancement in absorbance is due to light confinement around the edge of the AuND array and also enlarged light-matter interaction. Next, the measured PL spectra are shown in Figure 1f, illustrating that the PL of the AuND/ MoS_2 hybrid structure gets enhanced which may be due to strong light-matter interaction and plasmonic-induced resonance energy transfer (PIRET) effect.^{26, 37, 38}

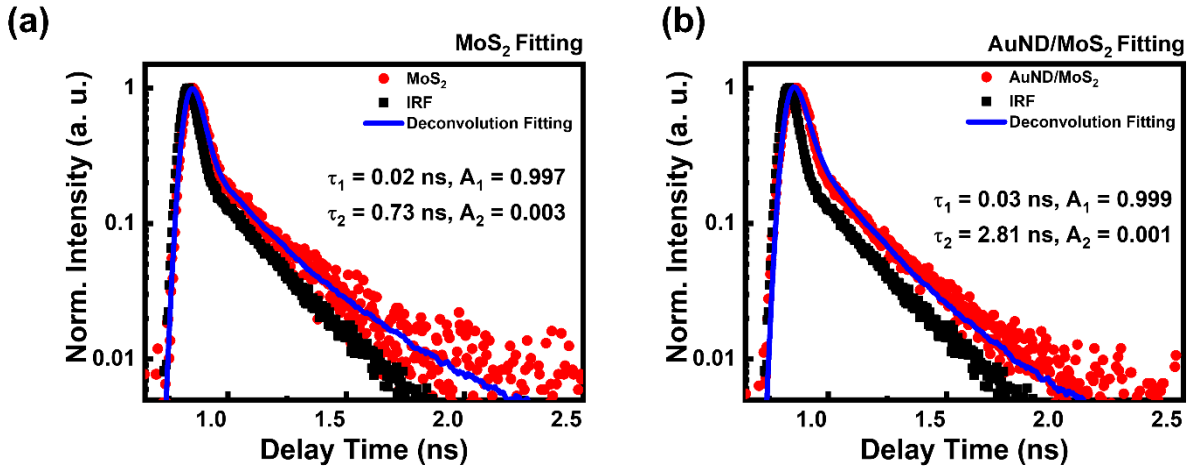


Figure 2: Time-resolved photoluminescence (TRPL) measurement (a) Fitted TRPL plot for MoS_2 , and (c) Fitted TRPL plot for AuND/ MoS_2 . Here TRPL data was fitted using bi-exponential decay function $f(t) = A_1 \exp^{-t/t_1} + A_2 \exp^{-t/t_2}$. Here, A_1 and A_2 are described by amplitude coefficient, and t_1 and t_2 for a short and long-lifetime corresponding to nonradiative and radiative recombination at surface trap states and band edge, respectively.

To further investigate the effect on excitons dynamics of MoS_2 due to the hybridization of the AuND array, we performed the time resolve photoluminescence (TRPL) spectroscopy (for

measurement details refer to **Experimental Methods**) as shown in **Figure 2**. The measured TRPL spectra were fitted using biexponential function $f(t) = A_1 \exp^{-t/t_1} + A_2 \exp^{-t/t_2}$. Here, A_1 and A_2 are described by amplitude coefficient, and t_1 and t_2 for short and long-lifetime correspond to nonradiative and radiative recombination at surface trap states and band edge, respectively.³⁹ The fitted TRPL plot for pristine MoS₂ and AuND/MoS₂ are exhibited in Figure 2a and Figure 2b, respectively. The calculated parameters after the biexponential fitting are shown in Table S1. (Supporting Information). The short (t_1) and long (t_2) lifetimes for MoS₂ were found to be 0.02 ns and 0.73 ns which is shorter than the 0.03 ns and 2.81 ns of AuNDs and MoS₂ hybrid structure. The average lifetime for AuND/MoS₂ is again 2.84 ns longer than of MoS₂ hybrid structure. This prolonged lifetime of excitons in the AuND/MoS₂ hybrid structure is due to trapping state passivation by hot electron injection from AuND to MoS₂ and strong resonance coupling between LSPR and exciton, resulting in the suppression of fast exciton recombination.⁴⁰

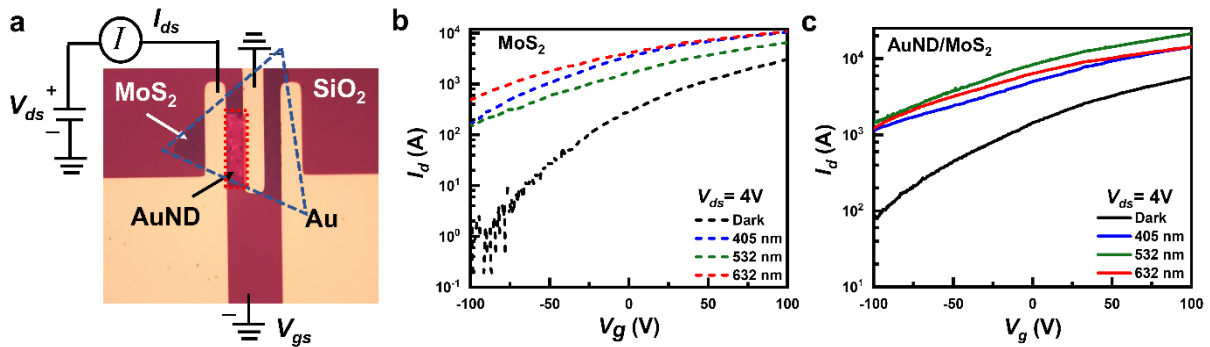


Figure 3: (a) The Optical microscope image of fabricated AuND/MoS₂ phototransistor with corresponding circuit diagram for transfer characteristic measurement. (b) I_d - V_g response for pristine MoS₂. (c) I_d - V_g response of AuND/MoS₂ phototransistor.

In addition to the optical characteristics, we further probe the electrical characteristics of MoS₂ and AuND/MoS₂ hybrid phototransistors. The fabrication of this hybridized phototransistor was carried out using a standard lithography technique (refer to Figure S3, Supporting Information for the device fabrication process). The optical microscope image of

the fabricated device with measurement schematic is shown in **Figure 3a**. The transfer characteristics of MoS₂ and AuND/MoS₂ are illustrated in Figure 3b and Figure 3c, respectively. The normal transfer characteristics are shown in Figure S4 (Supporting Information). The threshold voltage (V_{th}), defined by the intercept on V_{gs} with regression fitted line is calculated. The V_{th} for MoS₂ phototransistor is -42 V against the $V_{th} = -74.8$ V for the AuND/MoS₂ phototransistor, representing the increase in n-type doping after hybridization of AuND with MoS₂.¹⁷ This increase in n-type of doping may contribute due to hot electron transfer from AuNDs to MoS₂. In addition, the different incident wavelength shows different threshold voltage, indicating a wavelength-dependent electrical characteristic of the MoS₂ phototransistor. Further, it is observed that the drain current I_{ds} increased for AuND/MoS₂ phototransistors at fixed applied gate voltage. It may be attributed to the confinement of light near the vicinity of AuND and the enhanced population of photoexcited excitons.

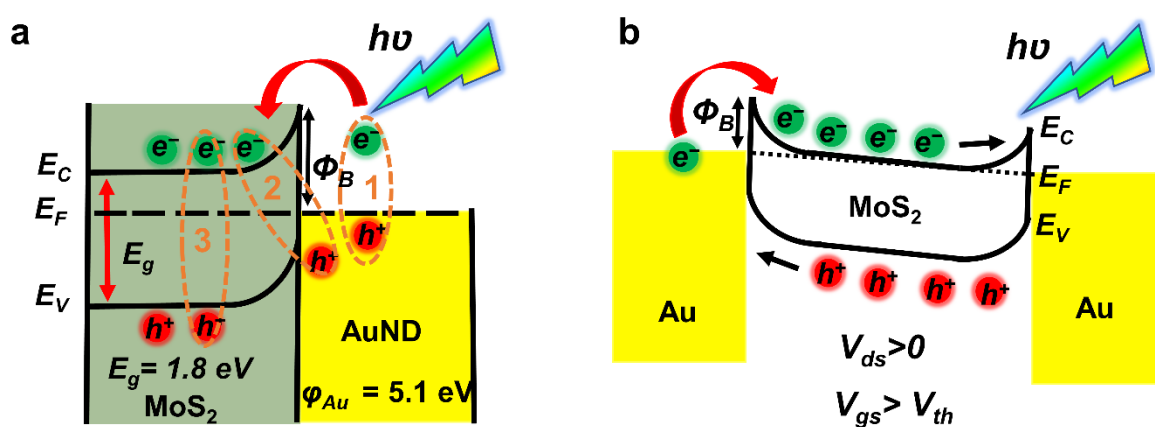


Figure 4: a) Energy band diagram of AuND/MoS₂ hybrid structure, representing when MoS₂ bring in the proximity of AuND they form a Schottky barrier with height Φ_B . A photoinduced plasmonic hot electron from AuND transfer to the conduction band of MoS₂, numbers 1, 2, and 3 represent plasmon-induced hot electron transfer, charge carrier transfer, and resonance energy transfer, respectively. b) Charge carrier transfer flow chart of MoS₂ under the applied bias $V_{ds} > 0$ V and gate voltage $V_{gs} > V_{th}$ under the incident light.

Next, to explain charge carrier generation and drift mechanism, **Figure 4** illustrates the energy band diagram of the AuND/MoS₂ hybrid structure without and with an applied bias. In Figure 4a, a single-layer MoS₂ with a Fermi energy of -4.6 eV,^{41, 42} and AuND with a work function of ≈ -5.1 eV, form a hybrid structure with a Schottky barrier of Φ_B , when they brought into the proximity. Next, when light incident on the hybrid structure three mechanisms take place simultaneously: (1) plasmon-induced hot electron from AuND transfer to MoS₂ and passivate the trap state at the interface.⁴³ (2) LSPR-induced charge carrier transfer directly to the conduction band of MoS₂. (3) photoinduced resonance energy transfer generates charge carriers directly in MoS₂.⁴⁴ In the absence of an external bias, the charge carriers are at their respective energy levels, resulting in zero net currents. However, upon applying an external bias V_{ds} across the electrodes, the photogenerated excitons get dissociated, and the charge carriers from MoS₂ begin to drift toward opposite potentials, as depicted in Figure 4b. This leads to a net current flow in contrast to the case when $V_{ds} = 0$ V.

Next, to evaluate the photo-sensing performance of the hybridized phototransistor, a biased voltage (V_{ds}) from 0-4 V was applied across the drain-source contacts to measure the drain current (I_d), under the constant back gate-source voltage of $V_{gs} = 100$ V with different illumination power and wavelengths. First, we compared the photocurrent response with applied bias voltage for pristine MoS₂, and AuND/MoS₂ with an illumination power at three wavelengths (405nm, 532 nm, and 632 nm) covering the entire visible spectrum of incident light. The photocurrent response for pristine MoS₂ and AuND/MoS₂ at 632 nm illumination wavelength is shown in Figure 5a, and Figure 5b, respectively. The photocurrents are enhanced by hybridizing AuND with MoS₂ at the same illumination power, as expected. Such a result stems from greater optical absorption, which is consistent with our optical measurements mentioned in Figure 1f & Figure S2b (Supporting Information). The photocurrent response with 405 nm and 532 nm laser illumination on MoS₂ and AuND/MoS₂ was also measured under the same condition and is shown in Figure S6 and Figure S7 (Supporting Information). The

photocurrent (I_{photo}) was calculated using ($I_{ph} = I_{light} - I_{dark}$). We observed that the device has a better photo response at 632 nm laser compared to that at 405 nm and 532 nm laser illumination. This better performance is due to high light harvesting at the resonance wavelength (exciton-plasmon coupling), consistent with UV-Visible spectra in Figure S2b.

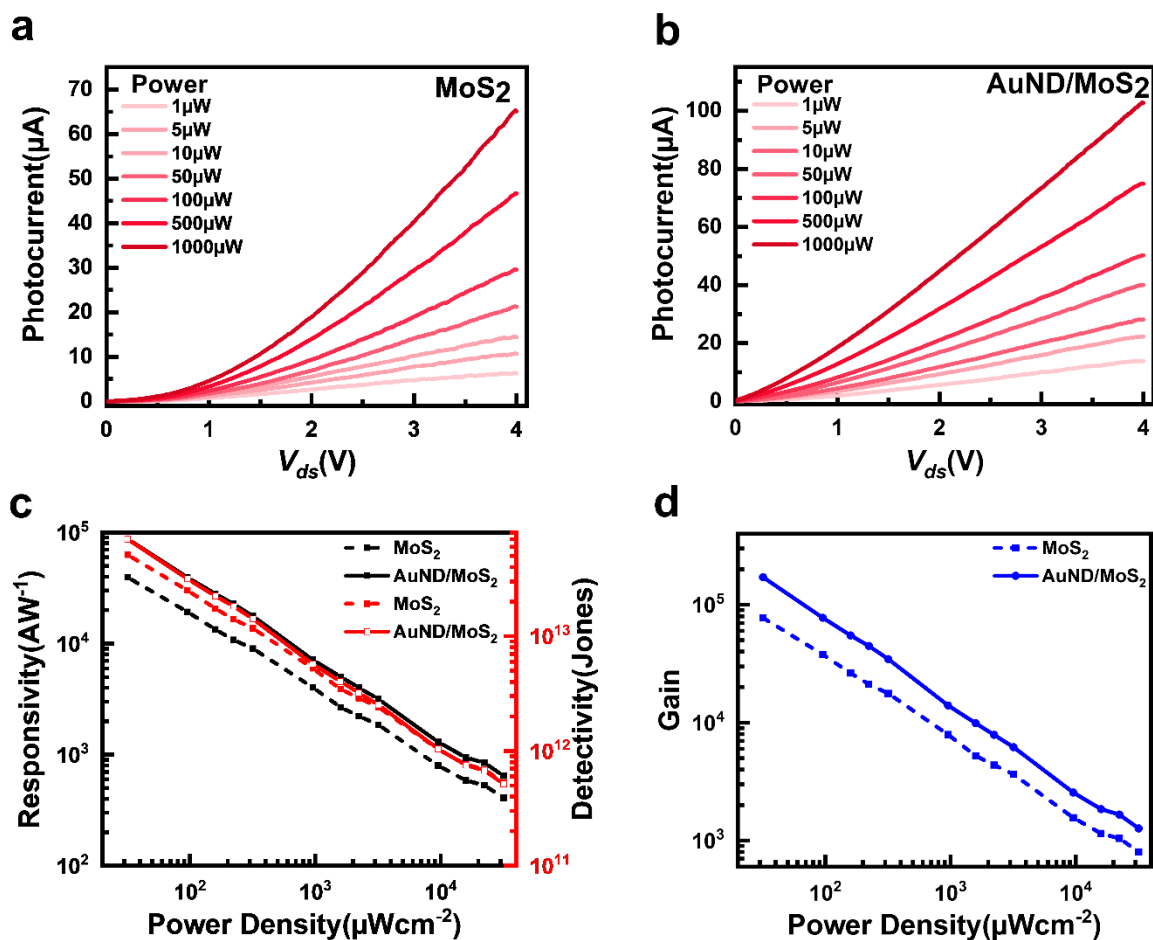


Figure 5: Optoelectrical Characterization: a,b) Photocurrent with applied bias V_{ds} at different illumination power for MoS₂ and AuND/MoS₂ phototransistors, respectively. c) responsivity and detectivity, d) gain with respect to the incident power density for MoS₂ AuND/MoS₂ phototransistor at applied bias voltage $V_{ds} = 4V$, of the incident wavelength of 632nm.

Second, we further studied the optoelectronic characteristics of MoS₂, and AuND/MoS₂ at the resonance wavelength in this work. The other two wavelengths are also provided in Figure S6c-d and Figure S7c-d (Supporting Information). As shown in Figures 5a and Figure 5b, the photocurrent increases with stronger illumination power, which can be interpreted by the

greater population of photoexcited excitons. Based on the measured power-dependent photocurrents, we can characterize three key performance parameters- photoresponsivity (R) and specific detectivity (D^*), and $Gain$, by the following equations,⁴⁵⁻⁴⁷

$$R = \frac{I_{ph}}{P} ; \quad (1)$$

$$D^* = \frac{R_\lambda}{\sqrt{\frac{2qI_{dark}}{A}}} ; \quad (2)$$

$$D^* = \frac{\sqrt{AB}}{NEP} ; \quad (3)$$

$$Gain = \frac{(hcR_\lambda)}{q\lambda} . \quad (4)$$

where I_{ph} , P , R_λ , q , I_{dark} , A , B , NEP , h , c , and λ denote photocurrent ($I_{ph} = I_{light} - I_{dark}$), illumination power, photoresponsivity at a wavelength of λ , charge, dark current, active area of the device, bandwidth, noise equivalent power, Planck constant, speed of the light, and wavelength, respectively.

$$NEP = \frac{I_N}{R} ; \quad (5)$$

Here, I_N is the noise current, and R is the responsivity of the photodetector. Further, I_N is defined as $I_N^2 = 2qI_D B$, where, I_D is the dark current, and B is the bandwidth.

The calculated R , D^* , and $Gain$ for both MoS₂ and AuND/MoS₂ are shown in Figure 5c–d. The R , D , and $Gain$ for other wavelengths are also shown in Figure S6c–d and Figure S6c–d (Supporting Information). Once again, among the two photodetectors, AuND/MoS₂ exhibits the best figure of merit (FOM, i.e., R , D^* and $Gain$) For example, the maximum responsivity, specific detectivity, and Gain of $8.7 \times 10^4 \text{ AW}^{-1}$, detectivity of $6.9 \times 10^{13} \text{ Jones}$, and gain 1.7×10^5 at $31.84 \mu\text{Wcm}^{-2}$ illumination power density of 632 nm wavelength with an applied voltage of 4.0 V. Note that it is a reasonable finding that both R and D^* decrease along with greater illumination power density, as shown in Figure 5c. Such decrease in the R and D^* can be attributed to saturation in optical absorption, the screening of the field by photoexcited carriers,

and enhanced carrier scattering rate.⁴⁸⁻⁵⁰ A similar trend was also observed in the calculated *Gain* presented in Figure 5d.

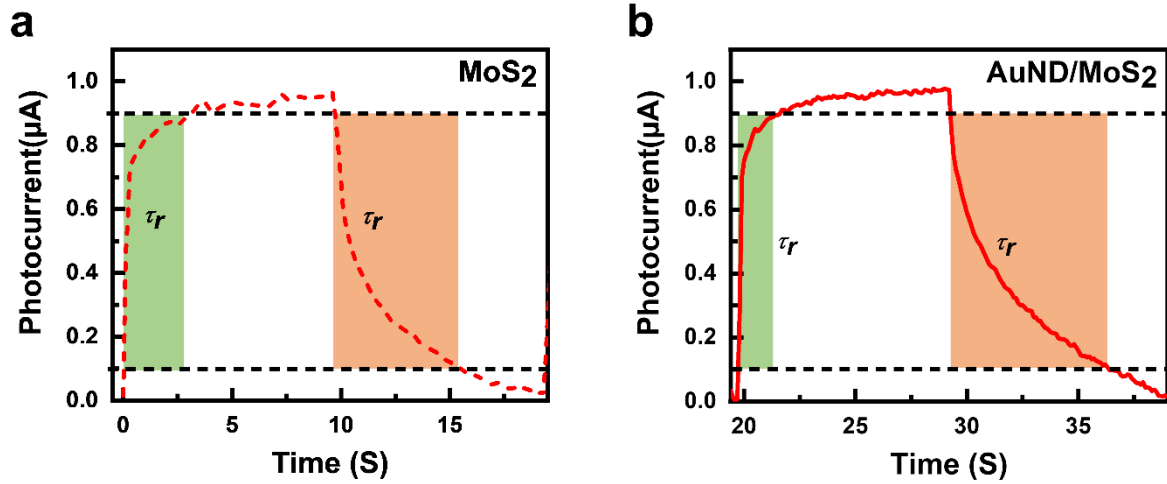


Figure 6: Transient photo response for a) the rise time 3.0 sec and fall time 5.8 sec. for MoS₂, b) the rise time 1.7 sec. and fall time 7.2-sec AuND/MoS₂ Phototransistor.

Finally, we probed the temporal response of this phototransistor. Both the rise time (C_r) and the fall time (C_f) are calculated by the time between 10 % to 90% of the maximum current. As shown in **Figure 6**, the C_r and C_f for AuND/MoS₂ are 1.7 s and 7.2 s, respectively, in contrast to those of pristine MoS₂ (3.0 s and 5.8 s). Such a reduction in the response times of this hybrid photodetector originates from the faster carrier excitation caused by the plasmonic effect of AuNDs. Furthermore, to investigate the spectral response of MoS₂ and AuND/MoS₂ photodetector, the photocurrent measurement with the same applied bias voltage and time at various illumination power of 432 nm and 532 nm wavelength is also performed (see Figure S6 and Figure S7, Supporting information). We observed that our designed AuND/MoS₂-based phototransistor shows broadband responses with a considerable optoelectronic performance which is supported by our UV-Vis measurement data. Consequently, we discovered that the designed AuND/MoS₂ hybrid photodetector achieved the highest responsivity of $8.7 \times 10^4 \text{ AW}^{-1}$, detectivity of $6.9 \times 10^{13} \text{ Jones}$, and Gain of 1.7×10^5 , at the illumination power density of $31.84 \mu\text{Wcm}^{-2}$ of 632 nm wavelength. The demonstrated device performance was also compared with

other reported works and is shown in Table 1 (supporting information) which is the highest up-to-date in this class of hybrid photodetectors.

3. Conclusions

In conclusion, we designed and fabricated AuND/MoS₂ hybrid phototransistor. Firstly, we characterized the optical properties of individual AuND, MoS₂, and their hybrids structures, and observed the synergetic effect from their hybrids. In particular, it is the AuND/MoS₂ that outperforms the foremost with the highest optical absorption and PL which is also confirmed by reflectance calculation using the FDTD technique. Secondly, Besides, by using time-resolve photoluminescence to study charge carrier dynamics, such a hybrid structure presented a prolonged charge carrier lifetime (2.84 ns). Finally, the hybrid phototransistor showed the synergy of optoelectronic effects. In particular, the AuND/MoS₂ hybrid phototransistor demonstrated the ultrahigh R , D^* , and $gain$ of $8.7 \times 10^4 \text{ AW}^{-1}$, $6.9 \times 10^{13} \text{ Jones}$, and 1.7×10^5 at $31.84 \mu \text{Wcm}^{-2}$ illumination power density of 632 nm wavelength with an applied voltage of 4.0 V, and R is the highest up to date in the same class of material-based photodetectors. This demonstrated hybrid photodetector shows a high potential to be used for optoelectronic applications.

4. Experimental Methods

Synthesis of monolayer MoS₂ by CVD methods and transfer process: CVD methods were used to produce a large area of monolayer MoS₂.^{51, 52} The CVD furnace consists of a single heat zone, and a 1-inch quartz tube is used as the reaction chamber. C-plane sapphire is used as substrate. MoO₃ powder and H₂S are used as the precursor and carrier gas. The first, system is pumped below 10^{-2} torr, where argon is used to purge the chamber. During growth, the furnace is heated to 400 °C in 10 minutes and maintained for 5 minutes, which is followed by the ramp to 900 °C in 15 minutes and maintained for 40 minutes for the growth of monolayer MoS₂. During the growth, O₂ is introduced starting from 800 °C. After completing, the furnace is subjected to fast cooling at 600 °C. The CVD-grown monolayer MoS₂ was then transferred using the wet

transfer methods.^{53, 54} Firstly, MoS₂/c-sapphire is coated with PMMA and dried at 65 °C for 1 hour. Next, the substrate near the interface was etched away with 1M potassium hydroxide (KOH) solution. Following that PMMA supported MoS₂ was rinsed three times in DI water to remove the base residues and then transferred to SiO₂/Si substrate. The target materials along with the substrate were dried under 65 °C for 3 hours for material adhesion and absorbed water removal. Finally, MoS₂ coated substrate was soaked in the acetone for 1 hour to get rid of PMMA. The optical microscope image and atomic force microscope image of transferred MoS₂ is shown in Figure S5a with a corresponding thickness of 0.7 nm which confirming CVD-grown MoS₂ is a monolayer.

Fabrication of Au disk array and Electrodes: Firstly, the gold electrodes on CVD-grown MoS₂ were patterned using digital lithography projection (DLP) tools followed by the development, Cr/Au (10/100 nm) deposition using electron beam evaporation, lift-off process. Next, for the fabrication of a gold nanodisk array, an electron beam lithography technique using Elionix ELS 7500-EX was used to expose to pattern Au nanodisk. The development process was done using a mixture of MIBK: IPA (1:3). The Au was deposited using electron beam evaporation methods followed by a liftoff process. The final device was annealed in an argon atmosphere at 150 °C for 2 hours to remove the absorbed moisture and other residual photoresists.

Numerical simulation: A commercial Lumerical software package was used to calculate the reflection spectra, and near electric field, distributions using the three-dimensional FDTD approach. A periodic boundary condition was applied with a mesh size of 0.3 nm over the x and y directions and a perfectly matched layer (PML) boundary condition was applied along the z direction. The plane wave source with the normal incident over 400 to 800 nm was used. The refractive index of Silicon, SiO₂, and Au (gold) was utilized from the reported data of Johnson and Christy⁵⁵.

Structural characterization: The structure parameter of fabricated Au nanodisk on MoS₂ coated SiO₂/Si substrate was examined utilizing field emission scanning electron microscopy (FESEM)

Hitachi SU 8010. The Optical Microscope was used to examine the patterned electrodes on MoS₂.

Optical measurements: Raman spectra of graphene have been collected using micro-Raman spectroscopy (HORIBA, LabRAM, HR800) with 532 nm solid-state laser excitation. The confocal laser scanning microscope system with a vibration-free closed-cycle cryostat (Attodry 800, attocube) was used to acquire the PL spectra. Through the employment of a 100x objective lens (0.82 NA; attocube), a 405 nm laser source as the excitation was focused to a small area (diameter ~ 1 μm) on the material. The same lens was used to record the PL emission spectra, which were then sent through a 405 nm long-pass filter and into a spectrometer (Andor, SR500i), which was composed of a monochromator and a thermoelectrically cooled CCD camera.

For TRPL measurements, the 400 nm excitation source was generated via SHG (second harmonic generation) in BBO crystal from an 800 nm pulsed laser (Tsunami, Spectra Physics) with a pulsed duration of 100 fs and a repetition rate of 1 kHz. A time-correlated single-photon counting (TCSPC) system (Pico Harp 300, Pico Quant) was employed to record the signal with a resulting time-resolution of 50 ps. Before the photon counting system, a 405 nm long-pass filter was used to remove any remaining light at 400 nm.

For micro UV-Visible spectra a were used to record the optical abortion of Au Nanodisk with MoS₂ and only MoS₂.

Optoelectrical measurements: To quantify the photoresponse of the fabricated devices, photoelectric measurements were conducted using a probe station system (Keithley, 2400 SCS). Lasers emitting at wavelengths of 405 nm, 532 nm, and 632 nm were employed within the visible spectrum to excite the AuND/MoS₂ phototransistor.

Author contributions

S.N.S. Yadav, and T.J Yen conceived the project. T.J Yen directed the project. S.N.S. Yadav designed the devices using FDTD simulation. S.N.S. Yadav fabricated and characterized it. Y.

C. Yao and Y. P. Hsieh synthesized large-area CVD MoS₂ and provide its Raman spectra. Y.-Y. Wang and Y.J. Lung performed the PL, TRPL, and micro UV-visible measurements. P.L. Chen and C.-H. Liu helped to measure optoelectronic characteristics. S.N.S. Yadav process all the data and analyzed it. All authors participated in the preparation of the manuscript and commented on its content.

Acknowledgments

This work was financially supported by the “High Entropy Materials Center” from The Featured Areas Research Center Program within the framework of the Higher Education Sprout Project by the Ministry of Education (MOE) and from the Project NSTC 111-2634-F-007-008 - by National Science and Technology Council (NSTC) in Taiwan.

Conflict of interest

All authors declare no conflict of interest.

Reference:

- (1) Mortazavi Zanjani, S. M.; Holt, M.; Sadeghi, M. M.; Rahimi, S.; Akinwande, D. 3D integrated monolayer graphene–Si CMOS RF gas sensor platform. *NPJ 2D Mater. Appl.* **2017**, *1* (1), 36.
- (2) Wu, F.; Tian, H.; Shen, Y.; Hou, Z.; Ren, J.; Gou, G.; Sun, Y.; Yang, Y.; Ren, T.-L. Vertical MoS₂ transistors with sub-1-nm gate lengths. *Nature* **2022**, *603* (7900), 259-264.
- (3) Manzeli, S.; Ovchinnikov, D.; Pasquier, D.; Yazyev, O. V.; Kis, A. 2D transition metal dichalcogenides. *Nat. Rev. Mater.* **2017**, *2* (8), 17033.
- (4) Das, S.; Sebastian, A.; Pop, E.; McClellan, C. J.; Franklin, A. D.; Grasser, T.; Knobloch, T.; Illarionov, Y.; Penumatcha, A. V.; Appenzeller, J.; et al. Transistors based on two-dimensional materials for future integrated circuits. *Nature Electronics* **2021**, *4* (11), 786-799.
- (5) Wang, Q. H.; Kalantar-Zadeh, K.; Kis, A.; Coleman, J. N.; Strano, M. S. Electronics and optoelectronics of two-dimensional transition metal dichalcogenides. *Nat. Nanotechnol.* **2012**, *7* (11), 699-712.
- (6) Mak, K. F.; Lee, C.; Hone, J.; Shan, J.; Heinz, T. F. Atomically Thin MoS_2 : A New Direct-Gap Semiconductor. *Phys. Rev. Lett.* **2010**, *105* (13), 136805.
- (7) Splendiani, A.; Sun, L.; Zhang, Y.; Li, T.; Kim, J.; Chim, C.-Y.; Galli, G.; Wang, F. Emerging Photoluminescence in Monolayer MoS₂. *Nano Lett.* **2010**, *10* (4), 1271-1275.
- (8) Kam, K. K.; Parkinson, B. A. Detailed photocurrent spectroscopy of the semiconducting group VIB transition metal dichalcogenides. *The Journal of Physical Chemistry* **1982**, *86* (4), 463-467.
- (9) Fivaz, R.; Mooser, E. Mobility of Charge Carriers in Semiconducting Layer Structures. *Physical Review* **1967**, *163* (3), 743-755.
- (10) Radisavljevic, B.; Radenovic, A.; Brivio, J.; Giacometti, V.; Kis, A. Single-layer MoS₂ transistors. *Nat. Nanotechnol.* **2011**, *6* (3), 147-150.

- (11) Lee, H. S.; Min, S.-W.; Chang, Y.-G.; Park, M. K.; Nam, T.; Kim, H.; Kim, J. H.; Ryu, S.; Im, S. MoS₂ Nanosheet Phototransistors with Thickness-Modulated Optical Energy Gap. *Nano Lett.* **2012**, *12* (7), 3695-3700.
- (12) Tsai, D.-S.; Liu, K.-K.; Lien, D.-H.; Tsai, M.-L.; Kang, C.-F.; Lin, C.-A.; Li, L.-J.; He, J.-H. Few-Layer MoS₂ with High Broadband Photogain and Fast Optical Switching for Use in Harsh Environments. *ACS Nano* **2013**, *7* (5), 3905-3911.
- (13) Lopez-Sanchez, O.; Lembke, D.; Kayci, M.; Radenovic, A.; Kis, A. Ultrasensitive photodetectors based on monolayer MoS₂. *Nat. Nanotechnol.* **2013**, *8* (7), 497-501.
- (14) Mak, K. F.; Shan, J. Photonics and optoelectronics of 2D semiconductor transition metal dichalcogenides. *Nat. Photonics* **2016**, *10* (4), 216-226.
- (15) Bernardi, M.; Palummo, M.; Grossman, J. C. Extraordinary Sunlight Absorption and One Nanometer Thick Photovoltaics Using Two-Dimensional Monolayer Materials. *Nano Lett.* **2013**, *13* (8), 3664-3670.
- (16) Kuc, A.; Zibouche, N.; Heine, T. Influence of quantum confinement on the electronic structure of the transition metal sulfide $T\text{S}_2$. *Phys. Rev. B* **2011**, *83* (24), 245213.
- (17) Zhang, W.; Huang, J.-K.; Chen, C.-H.; Chang, Y.-H.; Cheng, Y.-J.; Li, L.-J. High-Gain Phototransistors Based on a CVD MoS₂ Monolayer. *Adv. Mater.* **2013**, *25* (25), 3456-3461.
- (18) Lee, S.; Park, J.; Yun, Y.; Lee, J.; Heo, J. Enhanced Photoresponsivity of Multilayer MoS₂ Phototransistor Using Localized Au Schottky Junction Formed by Spherical-Lens Photolithography. *Adv. Mater. Interfaces* **2019**, *6* (8), 1900053.
- (19) Miao, J.; Hu, W.; Jing, Y.; Luo, W.; Liao, L.; Pan, A.; Wu, S.; Cheng, J.; Chen, X.; Lu, W. Surface Plasmon-Enhanced Photodetection in Few Layer MoS₂ Phototransistors with Au Nanostructure Arrays. *Small* **2015**, *11* (20), 2392-2398.
- (20) Lan, H.-Y.; Hsieh, Y.-H.; Chiao, Z.-Y.; Jariwala, D.; Shih, M.-H.; Yen, T.-J.; Hess, O.; Lu, Y.-J. Gate-Tunable Plasmon-Enhanced Photodetection in a Monolayer MoS₂ Phototransistor with Ultrahigh Photoresponsivity. *Nano Lett.* **2021**, *21* (7), 3083-3091.

- (21) Cheng, R.; Li, D.; Zhou, H.; Wang, C.; Yin, A.; Jiang, S.; Liu, Y.; Chen, Y.; Huang, Y.; Duan, X. Electroluminescence and Photocurrent Generation from Atomically Sharp WSe₂/MoS₂ Heterojunction p–n Diodes. *Nano Lett.* **2014**, *14* (10), 5590-5597.
- (22) Lee, C.-H.; Lee, G.-H.; van der Zande, A. M.; Chen, W.; Li, Y.; Han, M.; Cui, X.; Arefe, G.; Nuckolls, C.; Heinz, T. F.; et al. Atomically thin p–n junctions with van der Waals heterointerfaces. *Nat. Nanotechnol.* **2014**, *9* (9), 676-681.
- (23) Gonzalez Marin, J. F.; Unuchek, D.; Watanabe, K.; Taniguchi, T.; Kis, A. MoS₂ photodetectors integrated with photonic circuits. *NPJ 2D Mater. Appl.* **2019**, *3* (1), 14.
- (24) Flöry, N.; Ma, P.; Salamin, Y.; Emboras, A.; Taniguchi, T.; Watanabe, K.; Leuthold, J.; Novotny, L. Waveguide-integrated van der Waals heterostructure photodetector at telecom wavelengths with high speed and high responsivity. *Nat. Nanotechnol.* **2020**, *15* (2), 118-124.
- (25) Li, Z.; Hu, S.; Zhang, Q.; Tian, R.; Gu, L.; Zhu, Y.; Yuan, Q.; Yi, R.; Li, C.; Liu, Y.; et al. Telecom-Band Waveguide-Integrated MoS₂ Photodetector Assisted by Hot Electrons. *ACS Photonics* **2022**, *9* (1), 282-289.
- (26) Butun, S.; Tongay, S.; Aydin, K. Enhanced Light Emission from Large-Area Monolayer MoS₂ Using Plasmonic Nanodisc Arrays. *Nano Lett.* **2015**, *15* (4), 2700-2704.
- (27) Abid, I.; Bohloul, A.; Najmaei, S.; Avendano, C.; Liu, H. L.; Péchou, R.; Mlayah, A.; Lou, J. Resonant surface plasmon–exciton interaction in hybrid MoSe₂@Au nanostructures. *Nanoscale* **2016**, *8* (15), 8151-8159.
- (28) Petrić, M. M.; Kremser, M.; Barbone, M.; Nolinder, A.; Lyamkina, A.; Stier, A. V.; Kaniber, M.; Müller, K.; Finley, J. J. Tuning the Optical Properties of a MoSe₂ Monolayer Using Nanoscale Plasmonic Antennas. *Nano Lett.* **2022**, *22* (2), 561-569.
- (29) Shan, H.; Yu, Y.; Wang, X.; Luo, Y.; Zu, S.; Du, B.; Han, T.; Li, B.; Li, Y.; Wu, J.; et al. Direct observation of ultrafast plasmonic hot electron transfer in the strong coupling regime. *Light Sci. Appl.* **2019**, *8* (1), 9.

- (30) Li, J.; Ji, Q.; Chu, S.; Zhang, Y.; Li, Y.; Gong, Q.; Liu, K.; Shi, K. Tuning the photo-response in monolayer MoS₂ by plasmonic nano-antenna. *Sci. Rep.* **2016**, *6* (1), 23626.
- (31) Li, Y.; DiStefano, J. G.; Murthy, A. A.; Cain, J. D.; Hanson, E. D.; Li, Q.; Castro, F. C.; Chen, X.; Dravid, V. P. Superior Plasmonic Photodetectors Based on Au@MoS₂ Core–Shell Heterostructures. *ACS Nano* **2017**, *11* (10), 10321-10329.
- (32) Kumar, R.; Sharma, A.; Kaur, M.; Husale, S. Pt-Nanostrip-Enabled Plasmonically Enhanced Broad Spectral Photodetection in Bilayer MoS₂. *Adv. Opt. Mater.* **2017**, *5* (9), 1700009.
- (33) Li, G.; Song, Y.; Feng, S.; Feng, L.; Liu, Z.; Leng, B.; Fu, Z.; Li, J.; Jiang, X.; Liu, B.; et al. Improved Optoelectronic Performance of MoS₂ Photodetector via Localized Surface Plasmon Resonance Coupling of Double-Layered Au Nanoparticles with Sandwich Structure. *ACS Appl. Electron. Mater.* **2022**, *4* (4), 1626-1632.
- (34) Liu, K.-K.; Zhang, W.; Lee, Y.-H.; Lin, Y.-C.; Chang, M.-T.; Su, C.-Y.; Chang, C.-S.; Li, H.; Shi, Y.; Zhang, H.; et al. Growth of Large-Area and Highly Crystalline MoS₂ Thin Layers on Insulating Substrates. *Nano Lett.* **2012**, *12* (3), 1538-1544.
- (35) Lee, Y.-H.; Zhang, X.-Q.; Zhang, W.; Chang, M.-T.; Lin, C.-T.; Chang, K.-D.; Yu, Y.-C.; Wang, J. T.-W.; Chang, C.-S.; Li, L.-J.; et al. Synthesis of Large-Area MoS₂ Atomic Layers with Chemical Vapor Deposition. *Adv. Mater.* **2012**, *24* (17), 2320-2325.
- (36) Liang, L.; Meunier, V. First-principles Raman spectra of MoS₂, WS₂ and their heterostructures. *Nanoscale* **2014**, *6* (10), 5394-5401.
- (37) Li, J.; Cushing, S. K.; Meng, F.; Senty, T. R.; Bristow, A. D.; Wu, N. Plasmon-induced resonance energy transfer for solar energy conversion. *Nat. Photonics* **2015**, *9* (9), 601-607.
- (38) Cushing, S. K.; Li, J.; Meng, F.; Senty, T. R.; Suri, S.; Zhi, M.; Li, M.; Bristow, A. D.; Wu, N. Photocatalytic Activity Enhanced by Plasmonic Resonant Energy Transfer from Metal to Semiconductor. *J. Am. Chem. Soc.* **2012**, *134* (36), 15033-15041.

- (39) Kumar, P. N.; Deepa, M.; Ghosal, P. Low-Cost Copper Nanostructures Impart High Efficiencies to Quantum Dot Solar Cells. *ACS Appl. Mater. Interfaces* **2015**, *7* (24), 13303-13313.
- (40) Seo, D.-B.; Trung, T. N.; Kim, D.-O.; Duc, D. V.; Hong, S.; Sohn, Y.; Jeong, J.-R.; Kim, E.-T. Plasmonic Ag-Decorated Few-Layer MoS₂ Nanosheets Vertically Grown on Graphene for Efficient Photoelectrochemical Water Splitting. *Nano-Micro Letters* **2020**, *12* (1), 172.
- (41) Haider, G.; Roy, P.; Chiang, C.-W.; Tan, W.-C.; Liou, Y.-R.; Chang, H.-T.; Liang, C.-T.; Shih, W.-H.; Chen, Y.-F. Electrical-Polarization-Induced Ultrahigh Responsivity Photodetectors Based on Graphene and Graphene Quantum Dots. *Adv. Funct. Mater.* **2016**, *26* (4), 620-628.
- (42) Bera, K. P.; Haider, G.; Usman, M.; Roy, P. K.; Lin, H.-I.; Liao, Y.-M.; Inbaraj, C. R. P.; Liou, Y.-R.; Kataria, M.; Lu, K.-L.; et al. Trapped Photons Induced Ultrahigh External Quantum Efficiency and Photoresponsivity in Hybrid Graphene/Metal-Organic Framework Broadband Wearable Photodetectors. *Adv. Funct. Mater.* **2018**, *28* (51), 1804802.
- (43) Wang, W.; Klots, A.; Prasai, D.; Yang, Y.; Bolotin, K. I.; Valentine, J. Hot Electron-Based Near-Infrared Photodetection Using Bilayer MoS₂. *Nano Lett.* **2015**, *15* (11), 7440-7444.
- (44) Linic, S.; Christopher, P.; Ingram, D. B. Plasmonic-metal nanostructures for efficient conversion of solar to chemical energy. *Nat. Mater.* **2011**, *10* (12), 911-921.
- (45) Manga, K. K.; Wang, S.; Jaiswal, M.; Bao, Q.; Loh, K. P. High-Gain Graphene-Titanium Oxide Photoconductor Made from Inkjet Printable Ionic Solution. *Adv. Mater.* **2010**, *22* (46), 5265-5270.
- (46) Konstantatos, G.; Sargent, E. H. Nanostructured materials for photon detection. *Nat. Nanotechnol.* **2010**, *5* (6), 391-400.
- (47) Koppens, F. H. L.; Mueller, T.; Avouris, P.; Ferrari, A. C.; Vitiello, M. S.; Polini, M. Photodetectors based on graphene, other two-dimensional materials and hybrid systems. *Nat. Nanotechnol.* **2014**, *9* (10), 780-793.

- (48) Chang, T.-Y.; Chen, P.-L.; Yan, J.-H.; Li, W.-Q.; Zhang, Y.-Y.; Luo, D.-I.; Li, J.-X.; Huang, K.-P.; Liu, C.-H. Ultra-Broadband, High Speed, and High-Quantum-Efficiency Photodetectors Based on Black Phosphorus. *ACS Appl. Mater. Interfaces*. **2020**, *12* (1), 1201-1209.
- (49) Yu, W. J.; Liu, Y.; Zhou, H.; Yin, A.; Li, Z.; Huang, Y.; Duan, X. Highly efficient gate-tunable photocurrent generation in vertical heterostructures of layered materials. *Nat. Nanotechnol.* **2013**, *8* (12), 952-958.
- (50) Britnell, L.; Ribeiro, R. M.; Eckmann, A.; Jalil, R.; Belle, B. D.; Mishchenko, A.; Kim, Y. J.; Gorbachev, R. V.; Georgiou, T.; Morozov, S. V.; et al. Strong Light-Matter Interactions in Heterostructures of Atomically Thin Films. *Science* **2013**, *340* (6138), 1311-1314.
- (51) Chen, W.; Zhao, J.; Zhang, J.; Gu, L.; Yang, Z.; Li, X.; Yu, H.; Zhu, X.; Yang, R.; Shi, D.; et al. Oxygen-Assisted Chemical Vapor Deposition Growth of Large Single-Crystal and High-Quality Monolayer MoS₂. *J. Am. Chem. Soc.* **2015**, *137* (50), 15632-15635.
- (52) Wang, Q.; Li, N.; Tang, J.; Zhu, J.; Zhang, Q.; Jia, Q.; Lu, Y.; Wei, Z.; Yu, H.; Zhao, Y.; et al. Wafer-Scale Highly Oriented Monolayer MoS₂ with Large Domain Sizes. *Nano Lett.* **2020**, *20* (10), 7193-7199.
- (53) Ma, D.; Shi, J.; Ji, Q.; Chen, K.; Yin, J.; Lin, Y.; Zhang, Y.; Liu, M.; Feng, Q.; Song, X.; et al. A universal etching-free transfer of MoS₂ films for applications in photodetectors. *Nano Research* **2015**, *8* (11), 3662-3672.
- (54) Watson, A. J.; Lu, W.; Guimarães, M. H. D.; Stöhr, M. Transfer of large-scale two-dimensional semiconductors: challenges and developments. *2d Mater.* **2021**, *8* (3), 032001.
- (55) Johnson, P. B.; Christy, R. W. Optical Constants of the Noble Metals. *Phys. Rev. B* **1972**, *6* (12), 4370-4379.

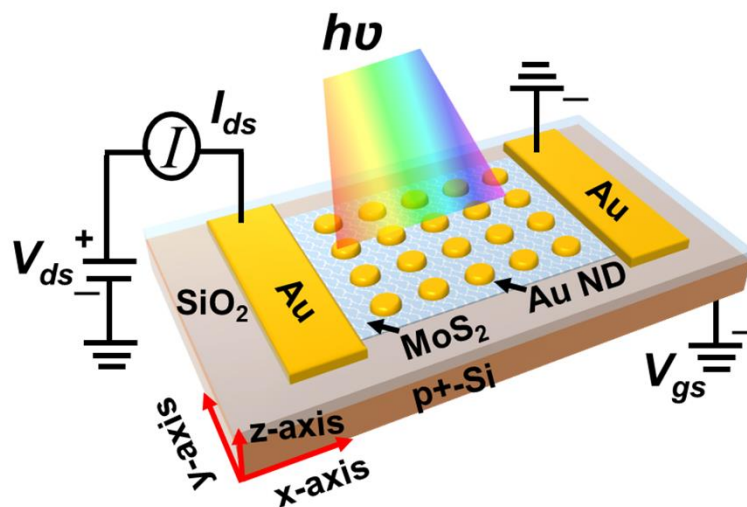
Table of contents:

To take advantage of the excitons-plasmon coupling of MoS₂ and AuND array, a hybrid structure has been developed. The incorporation of the AuND array in MoS₂ enhanced optical characteristics by intensifying the light-matter interaction via localized surface plasmon resonance. In addition, AuNDs also passivate the trap state of MoS₂ resulting in a delay in carrier decay. The demonstrated photodetector outperforms this class of photodetector and achieved the highest optoelectronic performance.

Keywords: MAPbBr₃ perovskite quantum dots, morphologically controlled gold nanocrystals, graphene, hybrid photodetector

Shyam Narayan Singh Yadav¹, Po-Liang Chen², Yu-Chi Yao³, Yen-Yu Wang^{6,7}, Der-Hsien Lien⁵, Yu-Jung Lu^{6,7}, Ya-Ping Hsieh³, Chang-Hua Liu^{2,4}, and Ta-Jen Yen^{1}*

Ultrahigh Photoresponsivity of Gold Nanodisk Array/CVD MoS₂-based Hybrid Phototransistor



Supporting Information

Ultrahigh Photoresponsivity of Gold Nanodisk Array/CVD MoS₂-based Hybrid Phototransistor

Shyam Narayan Singh Yadav¹, Po-Liang Chen², Yu-Chi Chen³, Yen-Yu Wang^{6,7}, Chang Hua Liu^{2,4}, Ya-Ping Hsieh³, Der-Hsien Lien⁵, Yu-Jung Lu^{6,7}, and Ta-Jen Yen^{1*}

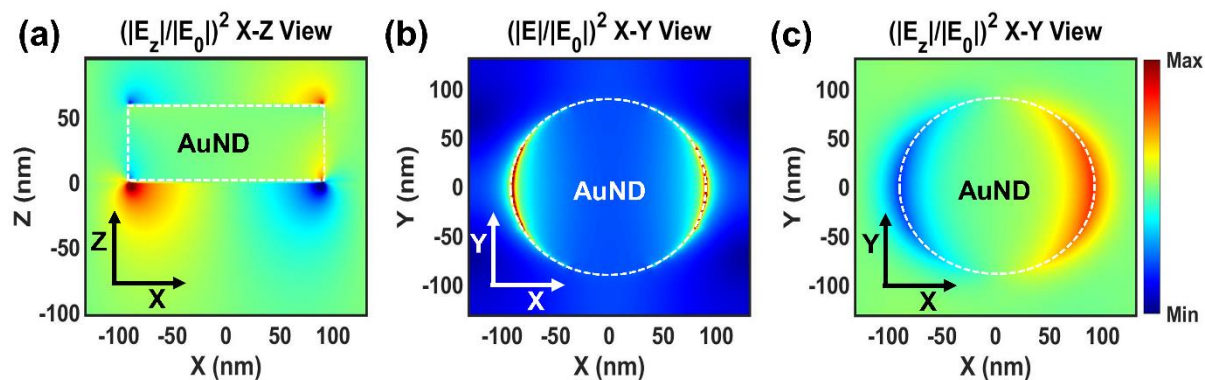


Figure S1: Electric field distribution for AuND in (a) X-Z view, (b) X-Y view, and (c) Z component in X-Y view.

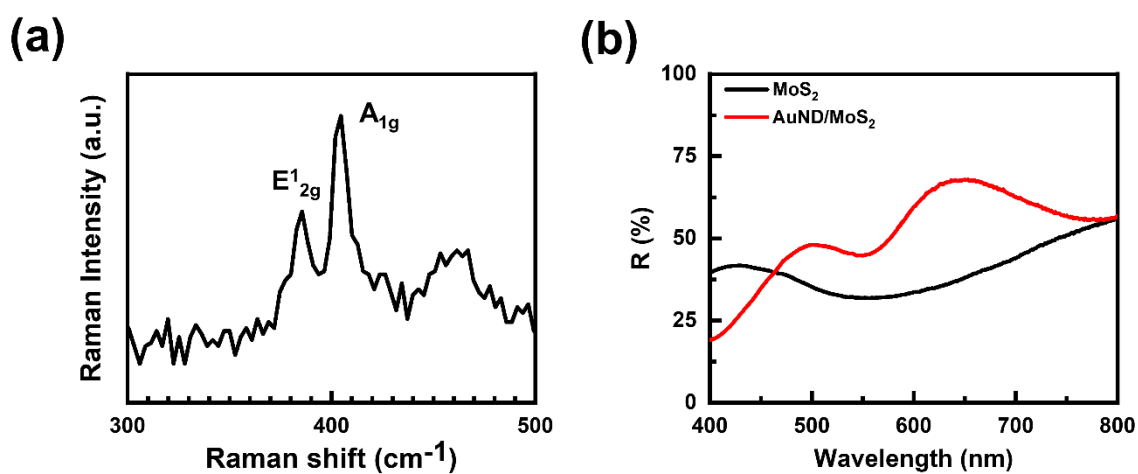


Figure S2: (a) Raman spectra of CVD-grown monolayer MoS₂, and (b) Reflectance spectra of MoS₂ and AuND/MoS₂.

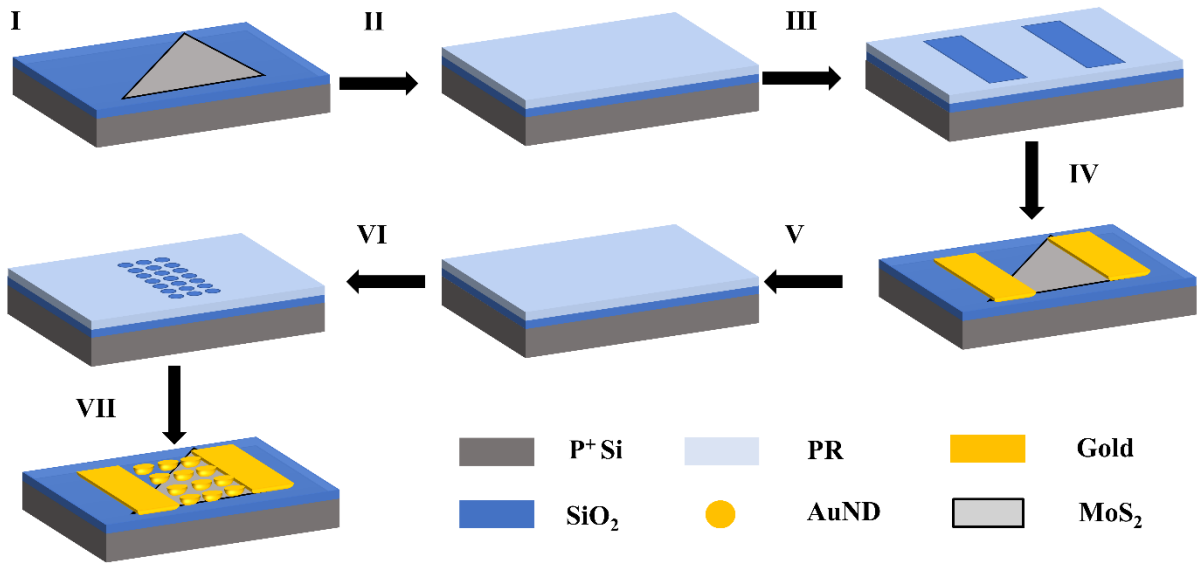


Figure S3: Device Fabrication Process flow (I) Transferred MoS₂ on SiO₂/Si substrate, (II) PR coating, (III) electrode patterned using digital lithography projection (DLP) system and developed, (IV) Au deposition using e gun evaporation system and liftoff (V) PR coating using spin coating system (VI) electron beam lithography for AuND array and development, (VII) Au deposition using e gun evaporation system and liftoff.

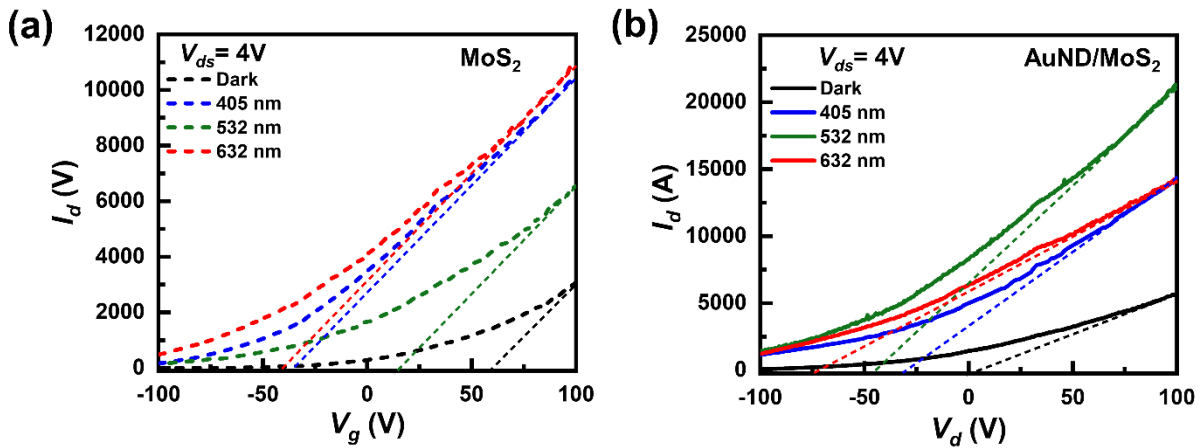


Figure S4: Transfer characteristic curve of (a) MoS₂, and (b) AuND/MoS₂. Here, dotted lines are tangents of the characteristic curve.

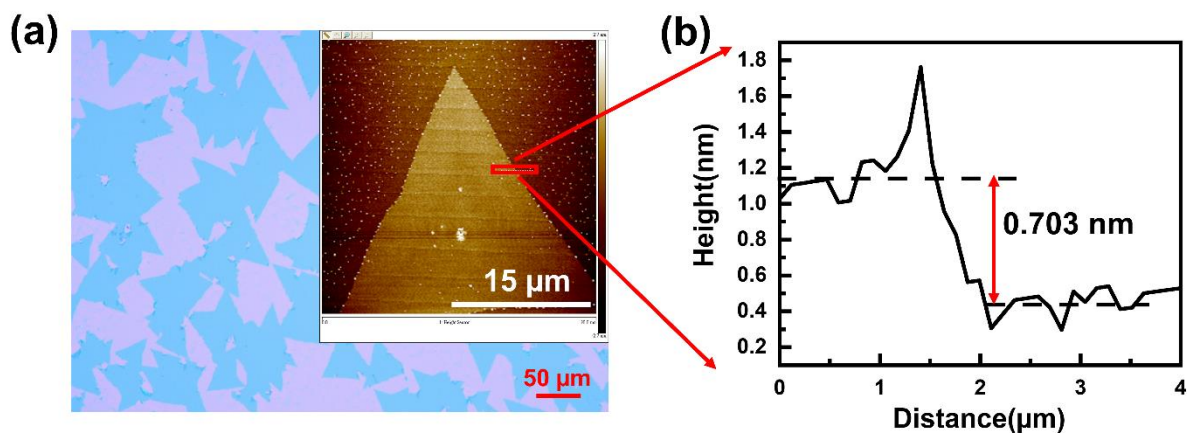


Figure S5: (a) Optical Microscope image of CVD-grown MoS₂, the inset image is an AFM image of a single flake of MoS₂. (b) the height profile of a single flake.

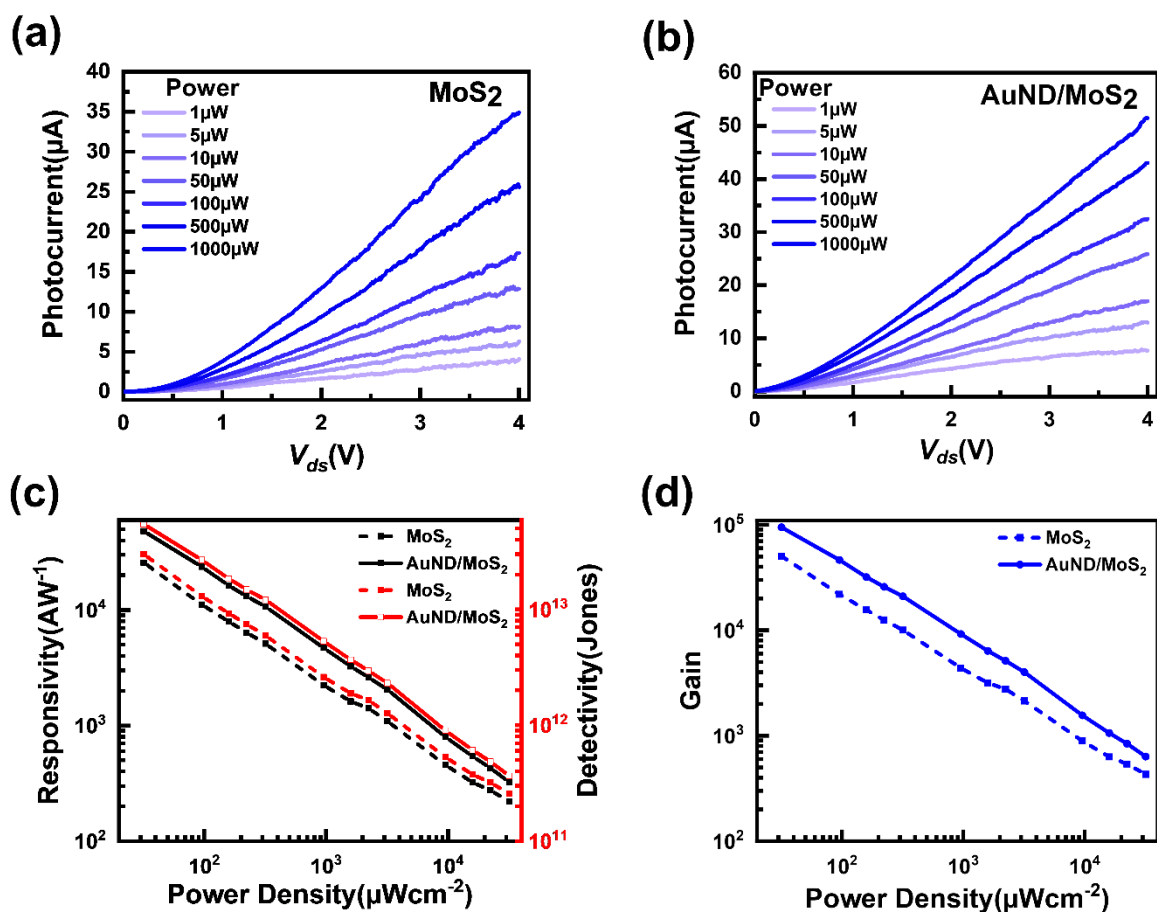


Figure S6. Optoelectrical Characterization: (a,b) Photocurrent with applied bias V_{ds} at different illumination power for MoS₂ and AuND/MoS₂ phototransistors, respectively. (c) responsivity and detectivity, (d) gain with respect to the incident power density for MoS₂

AuND/MoS₂ phototransistor at applied bias voltage $V_{ds} = 4V$, of the incident wavelength of 405 nm.

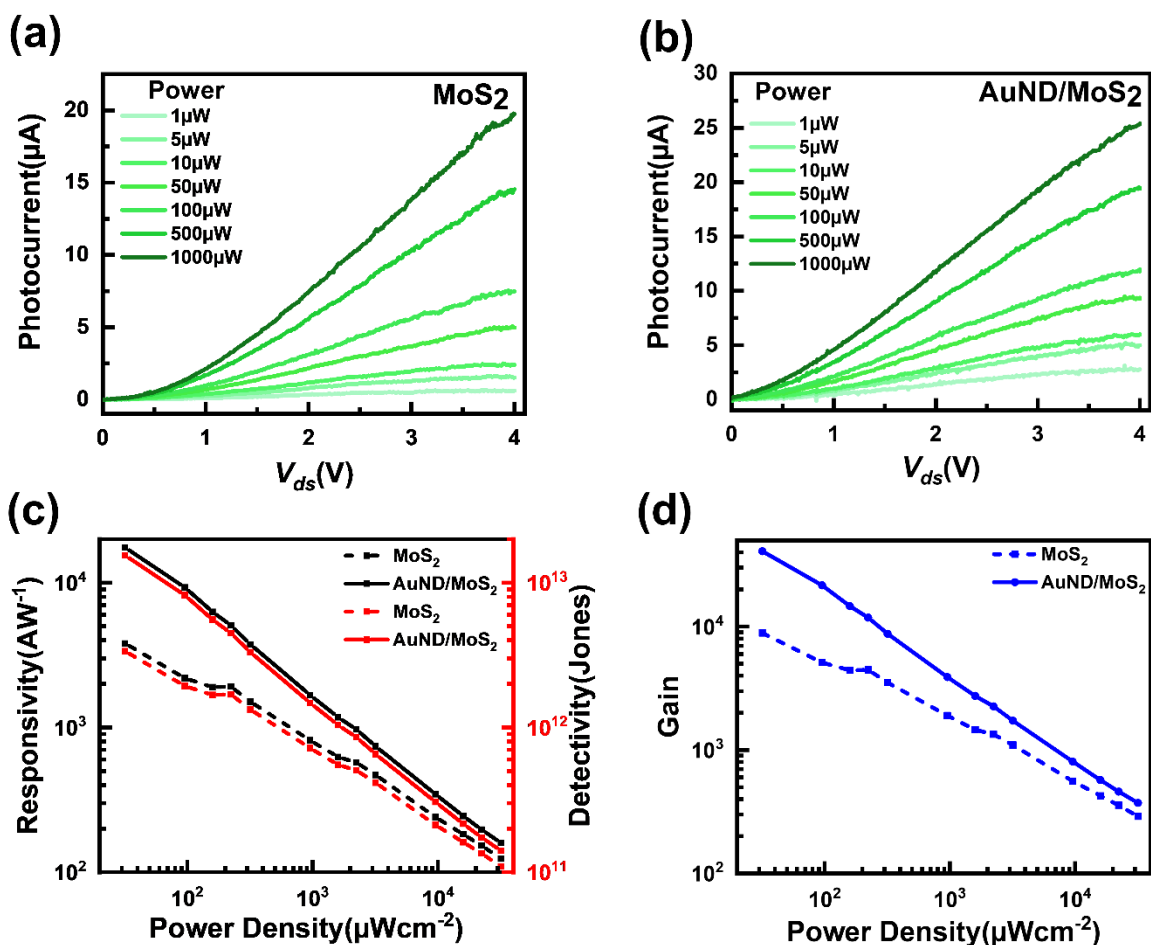


Figure S7. Optoelectrical Characterization: (a,b) Photocurrent with applied bias V_{ds} at different illumination power for MoS₂ and AuND/MoS₂ phototransistors, respectively. (c) responsivity and detectivity, (d) gain with respect to the incident power density for MoS₂ AuND/MoS₂ phototransistor at applied bias voltage $V_{ds} = 4V$, of the incident wavelength of 532nm.

Table S1. The calculated parameters after biexponential fitting of measured TRPL data

Type of Photodetector	A_1	t_1 [ns]	A_2	t_2 [ns]
MoS ₂	0.997	0.02	0.003	0.73
AuND/MoS ₂	0.999	0.03	0.001	2.81

CS1. The calculation of device parameters (Responsivity (R), External quantum efficiency (EQE), and specific detectivity (D^*) for AuND/MoS₂-based Phototransistor

The AuND/MoS₂-based phototransistor device parameters were obtained under an illuminating wavelength of 400-700 nm with 1 μ W (0.15 nW) 31.84713 μ Wcm⁻¹ power and an applied bias voltage of 4 V.

The **photoresponsivity (R)** for AuND/MoS₂-based phototransistor can be estimated using Equation 1;

$$R = \frac{|I_{photo}|}{P}; \quad (1)$$

where I_{photo} is the photocurrent ($I_{photo} = I_{light} - I_{dark}$), and, P is the illuminated power to the device [(laser power/laser spot area) \times device active area].

$$R = (13911.64016 \text{ nA}) / (1000\text{nW} \times 500 \mu\text{m}^2 / (3.14 \times 1 \times 10^6 \mu\text{m}^2)) = \mathbf{8.7 \times 10^4 \text{ AW}^{-1}}$$

The specific detectivity (D^*) of the AuND/MoS₂-based phototransistor-based photodetector can be calculated using Equation 2;

$$D^* = \frac{R_\lambda}{\sqrt{\frac{2qI_{dark}}{A}}}; \quad (2)$$

where R_λ , q , I_{dark} , and A , denote the responsivity at a wavelength of λ , charge, dark current, and active area of the device, respectively. The active area of the device was measured to be 9490 μm^2 .

$$D^* = 8.7 \times 10^4 \text{ AW}^{-1} \times (500 \times 10^{-8} \text{ cm}^2)^{1/2} / (2 \times 1.6 \times 10^{-19} \times 24.38913 \times 10^{-6} \text{ A})^{1/2} = \mathbf{6.9 \times 10^{13}}$$

Jones

The specific detectivity (D^*) of the AuNDs/MoS₂-based PD can also be calculated using Equation 3;

$$D^* = \frac{\sqrt{AB}}{NEP}; \quad (3)$$

Where A is the active area, B is the bandwidth which is inversely proportional to response time, and NEP is noise equivalent power.

NEP can be expressed as Equation 4;

$$NEP = \frac{I_N}{R}; \quad (4)$$

Here, I_N is the noise current, and R is the responsivity of the photodetector. Further, I_N is defined as $I_N^2 = 2qI_D B$, where, I_D is the dark current, and B is the bandwidth.

Now $B = 1/C = 1/1.7 \text{ sec.} = \mathbf{0.5882 \text{ S}^{-1}}$

$I_N = (2 \times 1.6 \times 10^{-19} \times 24.38913 \times 10^{-6} \text{ A} \times 0.5882 \text{ S}^{-1})^{1/2} = \mathbf{2.14257 \times 10^{-12} \text{ A}}$

Next, NEP can be calculated by $NEP = 2.14257 \times 10^{-12} / 8.7365 \times 10^4 \text{ AW}^{-1} = \mathbf{2.452 \times 10^{-17} \text{ W}}$

Now, specific detectivity can be calculated as $D^* = (500 \times 10^{-8} \text{ cm}^2 \times 0.5882 \text{ S}^{-1})^{1/2} / (2.452 \times 10^{-17} \text{ W}^{-1}) = \mathbf{6.994 \times 10^{13} \text{ cm Hz}^{1/2} \text{ W}^{-1} \text{ (Jones)}}$

The **Gain** for AuND/MoS₂-based phototransistor-based photodetector can be calculated using Equation 2;

$$\text{Gain} = \frac{(hcR_\lambda)}{q\lambda}; \quad (2)$$

where h , c , R_λ , q , and λ , indicate the Planck constant, speed of the light, responsivity at a wavelength of λ , charge, and wavelength of the incident light, respectively.

Here, $hc/q = 1240$

Gain = $((8.7 \times 10^4 \text{ AW}^{-1} \times 1240) / 632 \text{ nm}) = \mathbf{1.7 \times 10^5}$

Table S2. The comparison table for the photoelectric performance of the various reported photodetectors with different configurations.

Type of Photodetector	Responsivity	Detectivity [Jones]	Gain	Response Time Rise time/Fall time	References
Au disk/MoS ₂	26.9 AW ⁻¹ at 420 nm	6 × 10 ¹⁰	—	—	18
Au Nanoparticle/MoS ₂	2-3 mAW ⁻¹ at 632 nm	—	—	—	19
CVD MoS ₂	2200 AW ⁻¹ at 0.4 V, 532 nm	—	5000	—	17
AgND/Exfoliated MoS ₂	2.7 × 10 ⁴ AW ⁻¹ at 0.1V, 632 nm	1.3 × 10 ¹²	—	—	20
AuND/MoS ₂ phototransistor	8.7 × 10 ⁴ AW ⁻¹ at 4V, 632 nm	6.9 × 10 ¹³	1.7 × 10 ⁵	1.7/7.2	This Work